# Temperature-dependent far-infrared reflectance of an epitaxial (BaTiO_{3})_{8}/(SrTiO_{3})_{4} superlattice

V. Železný, O. Caha, A. Soukiassian, D. G. Schlom, and X. X. Xi

Phys. Rev. B **95**, 214110 — Published 15 June 2017

DOI: 10.1103/PhysRevB.95.214110

# Temperature-dependent far-infrared reflectance of an epitaxial $(BaTiO_3)_8/(SrTiO_3)_4$ superlattice

V. Železný
*Institute of Physics, Academy of Sciences of the Czech Republic*
*Na Slovance 2, 182 21 Prague 8, Czech Republic**

O. Caha
*CEITEC and Department of Condensed Matter Physics,*
*Masaryk University, 61137 Brno, Czech Republic*

A. Soukiassian and D.G. Schlom
*Department of Materials Science and Engineering,*
*Cornell University, Ithaca, New York, 14853-1501, USA and*
*Kavli Institute at Cornell for Nanoscale Science, New York 14853, USA*

X.X. Xi
*Department of Physics, Temple University, Philadelphia, Pennsylvania 19122, USA*
(Dated: May 18, 2017)

Infrared reflectance spectra of the polar optic phonons in a $[(BaTiO_3)_8/(SrTiO_3)_4]_{50}$ superlattice over the temperature range 8 to 650 K are reported. The spectra exhibit lattice vibration features typical of the perovskite constituents, $BaTiO_3$ and $SrTiO_3$. Using the effective medium approximation for multilayers systems and a fitting procedure, we were able to successfully simulate the infrared reflectivity of the superlattice structures and extract the parameters and dielectric functions of the phonons. When applied at varying temperatures, this approach provides the parameters of the zone-center polar phonons and their temperature dependence. Comparing these results with x–ray diffraction we identified some anomalies in phonon behavior related to the phase transitions that the superlattice undergoes.

PACS numbers: 77.55.+f, 77.22.Ch, 77.80.Bh, 77.84.-s

## I. INTRODUCTION

Ferroelectrics have been extensively studied for their interesting physical properties and many potential technical applications exploiting these properties[1–3]. The useful properties offered by ferroelectrics are a promising avenue to provide the required size reduction and speed increase desired for future microelectronic devices[4]. For this purpose they are expected to be used in the form of homogenous thin films or superlattices. Their properties can be tuned to exceed their bulk counterparts by varying the chemical composition and applying strain. The latter possibility can be realized through the coupling of polarization to strain, which leads to the changes in the phase transition temperature and other properties.

Enhanced dielectric constant and remanent polarization have been reported in short-period two-component[5–7] and three-component[8,9] ferroelectric superlattices. $BaTiO_3/SrTiO_3$ (BTO/STO) superlattice structures have achieved a significant enhancement of physical properties compared to the single-crystal epitaxial films of $BaTiO_3$ (BTO), $SrTiO_3$ (STO), and $Ba_xSr_{1-x}TiO_3$ (BST-$x$)[10].

The behavior of superlattices is more complex than thin films. One layer can be under tensile and another under compressive strain as occurs for BTO and STO in the superlattices considered here. Biaxial strain can be imparted into a superlattice through the differences in the lattice parameters and thermal expansion of the superlattice components and the underlying substrate[11–14]. Such strain reduces the structural symmetry of the superlattice and promotes an out-of-plane polarization for compressive strain and an in-plane polarization for tensile strain. The magnitude of the strain and its temperature dependence can be monitored by x-ray diffraction[15–17]. Moreover, electrostatic boundary conditions at the interfaces are expected to play an important role[18]. These are the main reasons why these systems are so popular[19,20].

Lattice dynamics is of central importance for understanding the physical properties of ferroelectrics. In displacive ferroelectric systems, a key role is played by the lowest-frequency transverse optic phonon, the soft mode that corresponds to the fluctuation of the primary order parameter. As the critical temperature $T_c$ is approached the soft-phonon displacement pattern is frozen-in to form a new phase. The change of $T_c$ can be varied through polarization-strain coupling by imparted biaxial strain and can be used to tune dielectric and other properties. Elucidation of the soft mode properties in superlattices is thus one of the most important tasks for experiment and calculations.

Raman spectroscopy has been the most frequently used technique for investigating phonons in superlattices[21,22]. For ferroelectric thin films and superlattices such studies

were difficult to perform in the past because the signal coming from the substrate overwhelmed that from the superlattice. The problem has been recently solved using UV excitation that suppresses the substrate contribution because a strong absorption reduces the excitation penetration depth[23].

Infrared spectroscopy is a nondestructive and very effective tool for studying the lattice dynamics of ferroelectrics, but has been employed far less because the Reststrahlen bands are broad, the reflectivity in them is close to one, and fine structures cannot be seen. The problem with substrate signal was partly overcome a few years ago when rare-earth scandate single crystals, whose infrared spectra are quite distinct from the ferroelectric superlattices, were introduced as substrates[24–26]. The incident radiation couples directly to the order parameter (polarization) and this can be used for the direct extraction of the dielectric function and determination of the lattice dynamics parameters. The Lyddane-Sachs-Teller relation can then be used to determine the total contribution of phonons to the static permittivity of the material. With its different selection rules, infrared spectroscopy also represents a complement to Raman spectroscopy.

Ferroelectric superlattices can have large permittivity, which can be caused by the conductivity of charged defects at the interfaces between the superlattice layers[27,28]. In these cases direct microwave and low-frequency dielectric measurements are difficult and infrared spectroscopy can be a very useful tool to estimate intrinsic permittivity.

Here we report far-infrared reflectance measurements on an epitaxial ferroelectric BTO/STO superlattice over a broad temperature range to fulfill the gap in experimental data. Using the effective medium approximation for the BTO/STO superlattice measured, we can determine the absolute value of the dielectric function and lattice dynamics parameters including the soft mode, which has up to now been difficult to obtain. The infrared measurement can be used to indicate phase transitions and their critical temperature, $T_C$, that can be compared and confirmed by x-ray scattering. Varying the temperature at which the spectroscopic measurements are made enables us to study the behavior of the soft mode in the vicinity of the phase transition in nanoscale ferroelectric heterostructures.

## II. EXPERIMENTAL

The infrared reflectance was measured on a fully commensurate $[(BaTiO_3)_8/(SrTiO_3)_4]_{50}$ superlattice, which was built up from 8 and 4 unit cell thick BTO and STO layers, respectively, repeated 50 times along the growth direction. They were grown by reactive molecular-beam epitaxy on the (110) surface of a $DyScO_3$ (DSO) substrate[29] using the nonstandard setting *Pbnm* for the substrate orientation. The superlattice growth was monitored using reflection high-energy electron diffraction (RHEED) oscillations. Following growth, the structural order and perfection was characterized by x-ray diffraction (XRD) and in some samples by high resolution transmission electron microscopy (HRTEM)[30]. XRD revealed excellent epitaxy and crystallinity in the superlattice samples, and HRTEM images showed atomically sharp BTO/STO interfaces and accurate periodicity[30]. For further details on sample growth and structural characterization please see Refs.[31,32] and the references therein.

The X-ray diffraction was used to measure the temperature dependence of the superlattice parameters. The experiment was performed using a Rigaku Smartlab x-ray diffractometer with a Cu-$K_\alpha$ copper anode radiation (wavelength 1.5406 Å), two-bounce germanium monochromator, and linear solid-state detector. A temperature series of symmetric scans was measured, where the positions of four substrate and numerous superlattice peaks were visible, allowing us to determine the out-of-plane lattice parameters of both the substrate and the average lattice parameter of the superlattice. In-plane lattice parameters were determined by measuring asymmetric diffraction peaks in two perpendicular directions. The temperature dependence of the lattice parameters was measured using an Anton Paar TTK 450 low-temperature chamber and a DHS 1100 high-temperature chamber.

Normal-incidence polarized infrared reflectance spectra were taken using a Fourier-transform spectrometer, (Bruker IFS 113v) equipped with a He-cooled bolometer. The low-temperature measurements in the temperature range from 8 to 300 K were done using a continuous-flow Optistat CF cryostat with polyethylene windows, which limited the spectral interval to 20 - 650 $cm^{-1}$. The high-temperature spectra from 300 to 650 K were measured in a furnace. Our room-temperature spectra were measured over a broader spectral range up to 3000 $cm^{-1}$, which enabled us to determine the high-frequency contribution from electronic transitions included in $\varepsilon_\infty$. The infrared reflectance was measured independently for the bare substrate as well as for a substrate covered with the superlattice in two polarizations: along the c-axis and perpendicular to it in the (110) plane of the DSO substrate.

Normal-incidence reflectance spectra from the bare substrate can be expressed as

$$R(\omega) = \left| \frac{\sqrt{\tilde{\varepsilon}(\omega)} - 1}{\sqrt{\tilde{\varepsilon}(\omega)} + 1} \right|^2 , \tag{1}$$

where the complex dielectric function $\tilde{\varepsilon}(\omega)$ is calculated using the Drude-Lorentz formula, which describes the contributions of all the $n$ modes lying in the plane of the sample surface as damped harmonic oscillators

$$\tilde{\varepsilon}(\omega) = \varepsilon_1(\omega) + i\varepsilon_2(\omega) = \varepsilon_\infty + \sum_{j=1}^{n} \frac{\omega_{Pj}^2}{\omega_{TOj}^2 - \omega^2 - i\omega\gamma_j} , \tag{2}$$

where $\omega_{TOj}$ is the transverse frequency of the $j$-th polar mode, $\omega_{Pj}$ is called its plasma frequency, $\gamma_j$ its damping constant, and the high-frequency permittivity $\varepsilon_\infty$ takes into account the contributions from higher energy optical transitions. The static permittivity is given by a sum of infrared-active phonons and electronic contributions

$$\varepsilon(0) = \varepsilon_\infty + \varepsilon_{ph} = \varepsilon_\infty + \sum_{j=1}^{n} \frac{\omega_{Pj}^2}{\omega_{TOj}^2} = \varepsilon_\infty + \sum_{j=1}^{n} \Delta\varepsilon_j \ , \quad (3)$$

where $\Delta\varepsilon_j = \omega_{Pj}^2/\omega_{TOj}^2$ is the contribution of the $j$-mode to $\varepsilon(0)$. In this way infrared spectroscopy can be used to provide a low-frequency estimate of dielectric permittivity.

As the penetration depth of the radiation is larger than the superlattice thickness, the substrate used displays considerable features in the reflectance spectrum. These features must be taken into account in the analysis. Each layer in the so-called three-medium "air-film-substrate" structure is modeled with the dielectric functions: $\varepsilon_1$=1 (air), $\varepsilon_2(\omega)$ (thin film), and $\varepsilon_3(\omega)$ (substrate). The total reflection coefficient at normal incidence for a structure with an epilayer of thickness $d$ is

$$\tilde{r}_{123} = \frac{\tilde{r}_{12} + \tilde{r}_{23}\exp(i2\beta)}{1 - \tilde{r}_{12}\tilde{r}_{23}\exp(i2\beta)} \ , \quad (4)$$

where $\tilde{r}_{ij} = (\tilde{n}_i - \tilde{n}_j)/(\tilde{n}_i + \tilde{n}_j)$ are Fresnel coefficients, $\tilde{n}_i = n_i + ik_i = \sqrt{\tilde{\varepsilon}_i}$ is the refractive index and its real and imaginary part, and $\beta = 2\pi d\omega\tilde{n}_2$ is a phase multiplier. The reflectance $R(\omega)$ is given by

$$R(\omega) = |\tilde{r}_{123}|^2 \quad (5)$$

Additional details can be found in Refs.[33–35].

An extension is made to apply the preceding approach for thin films to superlattices. Our superlattice supercell contains 12 perovskite formula units, has tetragonal $4mm$ symmetry, and its atomic vibrations are distributed among $47A_1 \oplus 12B_1 \oplus 59E$ irreducible representations[36]. 59 $E$ modes are infrared active and polarized in the plane of our superlattice and contribute to the dielectric function. The number of distinct polar modes in the superlattice structures is, however, too large, so that it is impossible to determine all of the polar mode frequencies from the experiment in this case. In order to overcome this principal difficulty and to calculate the dielectric function, we model the superlattice using an effective medium approach. Consider a superlattice formed by alternating layers of BTO and STO. The transverse electric field component must be continuous across the layer boundaries. In the long-wavelength limit and at normal incidence to the layers, the dielectric function may be written as a weighted average of the constituent materials.

$$\tilde{\varepsilon}_{SL}(\omega) = \frac{\tilde{\varepsilon}_{BTO}(\omega)d_{BTO} + \tilde{\varepsilon}_{STO}(\omega)d_{STO}}{d_{BTO} + d_{STO}} \ , \quad (6)$$

where $\tilde{\varepsilon}_{BTO}(\omega)$ and $\tilde{\varepsilon}_{STO}(\omega)$ are the dielectric functions and $d_{BTO}$ and $d_{STO}$ are the thicknesses of the superlattice layers.

## III. RESULTS AND DISCUSSION

### A. Structural characterization of $(BTO)_8/(STO)_4$ superlattices

X-ray diffraction shows that our superlattice has tetragonal $P4mm$ symmetry. The polarization lies along the [001], out-of-plane direction of the superlattice. The (001) plane of the BTO/STO superlattice surface is parallel to the (110) plane of the DSO substrate; the in-plane $[1\bar{1}0]$ and [001] directions of the DSO substrate are parallel to the [100] and [010] in-plane crystallographic directions of the BTO and STO components of the superlattice, respectively.

The lattice parameters of the DSO substrate ($Pbnm$ setting) are $a = 5.440$ Å, $b = 5.717$ Å, and $c = 7.903$ Å, respectively[37]. On the (110) surface a nearly perfect square lattice is formed with parameters $\sqrt{a^2 + b^2}/2 = 3.946$ Å along the $[1\bar{1}0]$ and $c/2 = 3.952$ Å along the [001] directions. They are matched with the STO (=3.905 Å) and BTO (with a pseudocubic spacing of 4.006 Å) lattices that are under nearly isotropic two-dimensional strain. The misfit, defined as $(a_{sub} - a_{film})/a_{film}$, between unstrained STO and BTO layers is 2.5% and in the superlattice on (110) DSO it is distributed as 1.1% tensile strain in the STO layers and 1.4% compressive strain in the BTO layers. The coherent tetragonal BTO/STO superlattice deposited on DSO substrate generates 1.1% tensile strain in STO layers and 1.2% compressive strain in BTO layers. The averaged in-plane lattice constant of the superlattice is only strained about 0.24% by the DSO substrate and this strain is much less in comparison to the internal strain in the superlattice.

The superlattice was characterized structurally using high-resolution x-ray diffraction. Reciprocal-space maps were collected to assess superlattice quality, i.e., commensurability, strain relaxation, and misfit dislocations. In-plane lattice parameters were measured by asymmetric reciprocal space maps in two perpendicular directions in the vicinity of substrate reciprocal lattice points 420 and 332. Reciprocal space maps at room and high temperature are plotted in Fig. 1, showing the superlattice peaks positioned in the same lateral position in reciprocal space as the substrate peaks, indicating an in-plane lattice match between the superlattice and the substrate that is independent of temperature.

A series of symmetric scans measured at different temperatures allowed us to determine the out-of-plane lattice parameters of both the substrate and the average lattice parameter of the superlattice. The results for both the in-plane and out-of-plane lattice parameters are plotted in Fig. 2 in the top and bottom panel, respectively.

The in-plane lattice parameters show only a linear coefficient of thermal expansion. The difference between the two orthogonal in-plane directions is a result of the pseudotetragonal symmetry of the substrate, where the lattice parameters and their thermal expansion behavior are not quite identical[38]. At high temperature, the

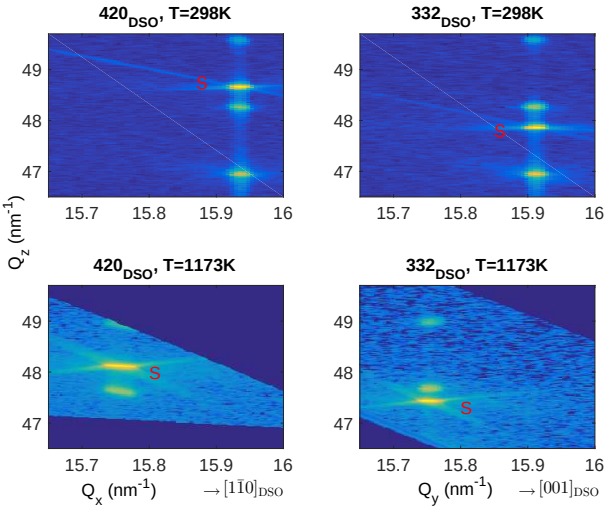


FIG. 1: (color online)Reciprocal space maps at room temperature (top) and at 1173 K (bottom) in the vicinity of the DSO 420 reflection (left) and the 332 reflection (right). Substrate peaks are denoted by the "S" label, $(BTO)_8/(STO)_4$ superlattice peaks are positioned above and below the substrate peak at the same $Q_x$ position, indicating that the BTO/STO superlattice is commensurately strained to the underlying DSO substrate.

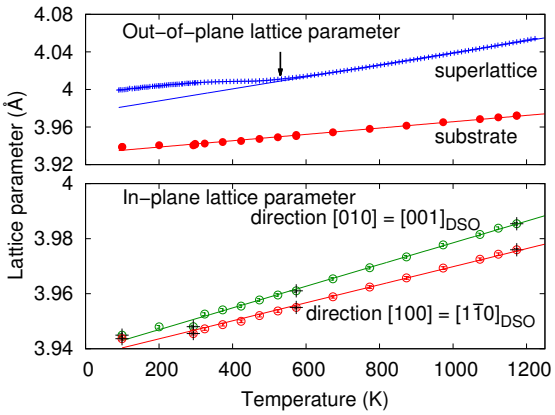


FIG. 2: (color online) Top: Temperature dependence of the average out-of-plane lattice parameter of the superlattice and interplanar distance of the (110) DSO substrate planes measured using x-ray diffraction. The lines are linear fits of the experimental data points at high temperature, showing that the out-of-plane lattice parameter of the superlattice deviates from a linear dependence below a temperature of about 550 K. Bottom: Temperature dependence of the in-plane lattice parameters of the superlattice along two perpendicular directions. Directions [100] and [010] are parallel to the [1$\bar{1}$0] and [001] crystallographic directions of the DSO substrate, respectively. The "+" symbols denote the measured in-plane lattice spacing of the DSO substrate, showing that the superlattice is commensurate over the entire temperature range.

out-of-plane lattice parameters of both the superlattice and the substrate show a similar linear dependence. Below about 550 K, however, significant deviation from this linear out-of-plane behavior is observed. This deviation is an indication of a phase transition. The superlattice is always clamped to the in-plane lattice spacing of the substrate. Further, the BTO and STO lattice parameters are clamped with a slight orthorhombic distortion because of the small difference between the in-plane lattice constants of DSO along its [1$\bar{1}$0] and [001] directions, which clamps the superlattice. Below 550 K an additional extension of the out-of-plane lattice parameter of the superlattice is added due to a ferroelectric phase transition, whose temperature is shifted higher than that of bulk $BaTiO_3$ as the whole system is biaxially strained. A similar effect was observed for a BTO thin film grown on a DSO substrate[17].

### B. Infrared spectroscopy of the $DyScO_3$ substrate

In order to extract the BTO/STO superlattice dielectric function and phonons parameters we first determine the infrared data and phonon parameters for the substrate and use them as a reference. DSO has an orthorhombic perovskite structure with four formula units per unit cell. Here a non-standard setting *Pbnm* was used, where $a < b < c$. Factor group analysis at the center of Brillouin zone gives the following decomposition into irreducible representations

$$\Gamma = 8B_{1u}(z) + 10B_{2u}(y) + 10B_{3u}(x) \qquad (7)$$

The decomposition gives 28 polar modes of which 25 are infrared active and three $(B_{1u} + B_{2u} + B_{3u})$ are acoustic. The analysis shows that $7B_{1u}$ phonons are polarized along the [001] direction while $9B_{2u}$ and $9B_{3u}$ phonons are polarized along the plane direction perpendicular to the *c*-direction, i.e., the [1$\bar{1}$0] direction. Normal incidence infrared reflectance measures the projections of these phonons onto the (110) surface plane. Such infrared reflectance spectra of the DSO substrate measured at room temperature in both polarizations are shown in Fig. 3: the electric field $E$ along the *c*-axis (panel a) and perpendicular to it (panel b). In the same figure the spectra of the $(BTO)_8/(STO)_4$ superlattice on (110) DSO and the spectra of the model fits are also shown for comparison. The substrate spectra show the expected typical phonon characteristics. They are similar to the spectra obtained by other authors[39–41], where further details about them can be found. All 7 modes predicted by the group analysis can be observed along the *c*-axis while only 14 modes are found in the direction perpendicular to it. This can be explained: some of them are weak, broadened or overlapping with each other, so they are difficult to be distinguished. The substrate reflectance, however, can be very well fitted using Eqs. 1 and 2 with 7 oscillators for the polarization along the *c*-axis and 14 oscillators perpendicular to it as it is also demonstrated in Fig. 3. The phonons in the whole family of bulk rare-earth scandates have been investigated using first-

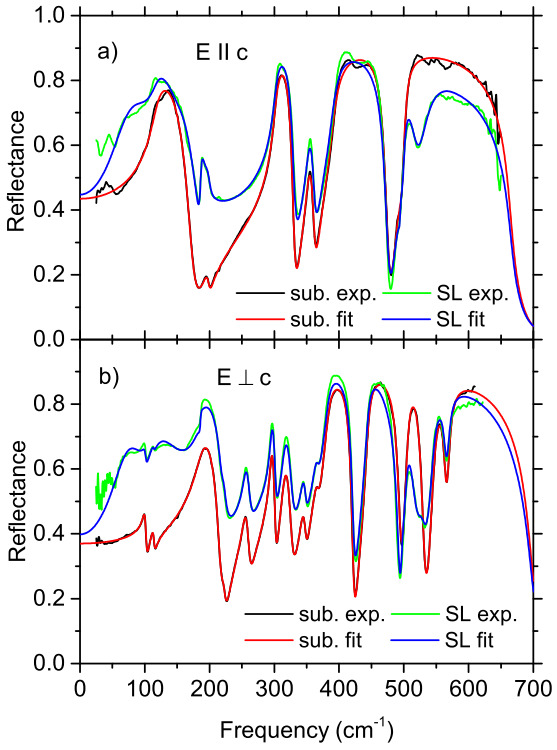


FIG. 3: (color online)Frequency dependence at room temperature of experimental and calculated reflectance spectra of a bare (110) DSO substrate and a (110) DSO substrate covered with the $(BTO)_8/(STO)_4$ superlattice for the polarization along the $c$-axis of DSO (panel a) and perpendicular to it along the $[1\bar{1}0]$ DSO direction (panel b). The labelling of the reflectance curves is following: sub. exp. - substrate experiment, sub. fit - substrate fit, SL exp. - superlattice experiment and SL fit - superlattice fit.

principles calculation[42] and the calculated phonons for DSO are in good agreement with our experimental data. On cooling, the DSO spectra show a typical enhancement in intensity and sharpening. This behavior and the interpretation of the spectra has been described in detail in the literature[39–41]; therefore we do not repeat it again here.

### C. Infrared spectroscopy of the $(BTO)_8/(STO)_4$ superlattice

The polarized reflectance spectra of the $(BTO)_8/(STO)_4$ superlattice with the polarizations parallel and perpendicular to the $c$-axis of DSO at room temperature are shown in Fig. 3. Obviously, most of the strong and sharp bands are common in all spectra and originate from the DSO substrate. The spectral features of the superlattice manifest themselves as differences between the reflectance of the superlattice on top of the substrate structure and that of the bare DSO substrate, as seen in Fig. 3 for both polarizations. Such clear signatures of three strong modes are near 80, 200 and 500 $cm^{-1}$ at room temperature. In the polarization along the $c$-axis, the lowest frequency mode is partly hidden by a strong reflection band coming from the substrate as it is seen in panel a.

The temperature dependence of the reflectance from 8 to 650 K is shown in Figs. 4 and 5. The spectra exhibit typical broadening with increasing temperature. The most interesting behavior of the reflectance in Fig. 5 can be observed at low frequency for the polarization $E \perp c$. The enhancement and development of the low frequency reflectance feature starts at 100 $cm^{-1}$ below 550 K, corresponding to the onset of the deviation of the out-of-plane lattice parameter in Fig. 2. The reflectance maximum shifts down to 70 $cm^{-1}$ as temperature is reduced to liquid helium temperature. The temperature development in the other polarization, $E \parallel c$, is shown in Fig. 4. The temperature dependence of the superlattice feature is here less apparent because it is overlaid by the strong reflectance from the substrate as it is mentioned above.

The cubic perovskite primitive cell with $m\bar{3}m$ $(O_h)$ point group symmetry contains 5 atoms and, therefore, there are 15 degrees of freedom. In the center of the Brillouin zone they are distributed among four optic phonons belonging to $3F_{1u} + 1F_{2u}$ irreducible representations. Each of these modes is triply degenerate and odd parity with respect to the space inversion, therefore, they are forbidden for first-order Raman scattering. The $F_{1u}$ modes are infrared active and are usually labeled as TO1, TO2, and TO4 modes, while the $F_{2u}$ mode is silent and labeled as the TO3 mode.

When the perovskite is transformed into the tetragonal phase (e.g. by phase transition, applied strain) all the $F_{1u}$ modes split into $A_1$ and $E$ modes, and the $F_{2u}$ phonon gives rise to $B_1$ and $E$ modes. The $A_1$-mode is polarized along the superlattice $c$-axis and the doubly degenerate $E$ modes are perpendicular to it. Our superlattice is grown with its $c$-axis perpendicular to the plane of the substrate surface and our normal reflectance measurements, therefore, scan only the $E$ components of the TO phonons.

In order to extract the phonon parameters relevant for both the substrate and superlattice, it was necessary to employ a fitting procedure. For this purpose, we parameterized the dielectric function in the Drude-Lorentz form, Eq. 2, (the classical damped harmonic oscillator formula) for both the substrate and superlattice. First, we fit the reflectivity spectrum of the bare substrate, considering it as a semi-infinite medium as described in the previous paragraph using Eqs. 1 and 2. Then, we fixed all of the substrate parameters and added a top layer to the model corresponding to the superlattice. Three high-frequency modes at about 180, 490 and 530 cm-1 are sufficiently separated and vary only weekly and in a

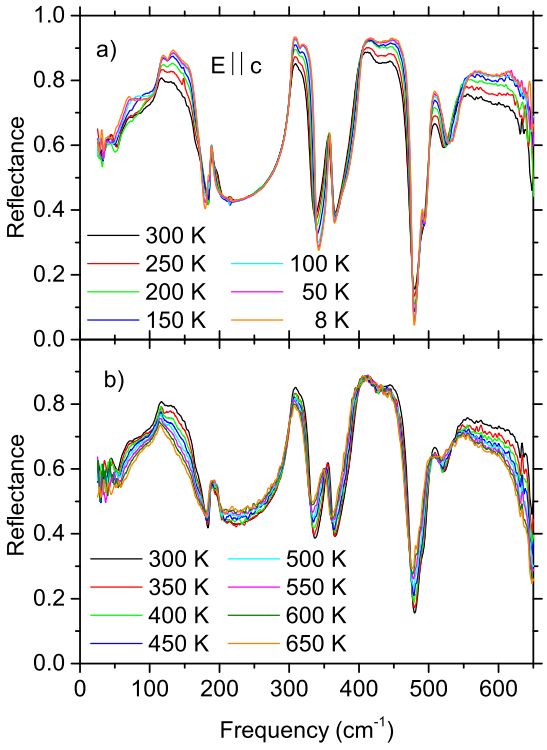


FIG. 4: (color online)Temperature dependence of the reflectance spectra of the $(BTO)_8/(STO)_4$ superlattice grown on (110) DSO with the polarization along the *c*-axis of the (110) DSO substrate for temperatures below room temperature a) and above room temperature b).

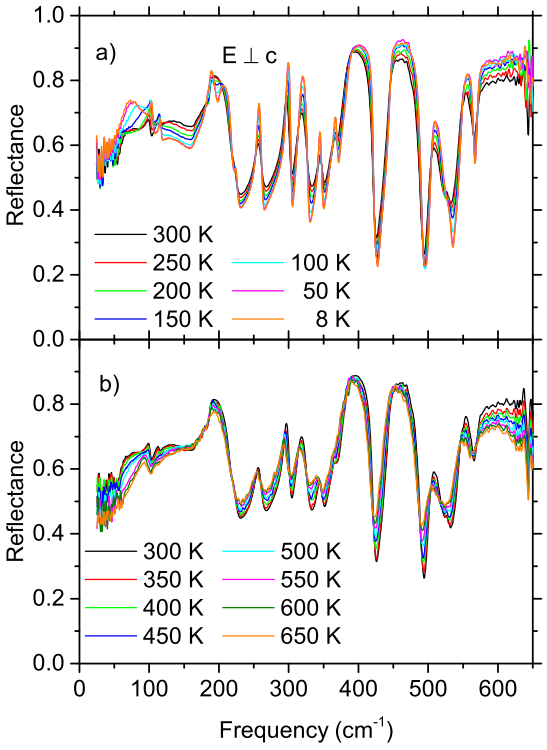


FIG. 5: (color online)Temperature dependence of the reflectance spectra of the $(BTO)_8/(STO)_4$ superlattice with the polarization perpendicular the *c*-axis of the (110) DSO substrate for temperatures below room temperature a) and above above b).

very regular way with temperature. So, it is easy to fit using Eqs. 4 and 5. More complicated situation occurs for low-frequency soft modes. It is possible, however, to distinguish two modes each on one side of the sharp doublet coming from substrate in this frequency range at room temperature. Then repeating this procedure step by step for other temperatures with the initial parameters taken from foregoing temperature , we get the parameters at all temperatures. In Fig. 5, the upper panel, it is possible to see that the mode intensity below the doublet increases and the mode intensity above the doublet decreases with decreasing temperature. Finally at 8 K, we get practically only one but a more enhanced mode. This behavior supports our fitting procedure. Fitting the two-layer system (semi-infinite substrate + superlattice) to the experimental spectrum using Eqs. 4 and 5, we were able to determine the effective parameters of the superlattice and consequently calculate all of its response functions. The good quality of our fitting procedure is illustrated in Fig. 3.

The frequency dependence of the superlattice dielectric function at selected temperatures is shown in Fig. 6. As the superlattice is a mixture of STO and BTO, the dielectric function consists of two groups of dispersion. These correspond to both constituent layers and their intensities are proportional to the concentration of constituents coming into the superlattice. Each dispersion is a sum of the *E*-components split from the original TO1, TO2, and TO4 polar phonons typical for perovskites. Such spectra can be successfully described within the concept of the effective medium approximation, Eq. 6, taking into account the 2:1 BTO/STO ratio.

The reflectance maximum corresponding to the lowest frequency phonon (the soft mode at about 80 $cm^{-1}$at room temperature) is quite smeared due to the major contribution from the heavily overdamped mode of the BTO component. At low temperature the mode becomes less damped and the reflectance maximum plays a much more significant role in the spectra. To describe the behavior of such peak it is necessary to use two oscillators. It is worth noting that no significant phonon frequency shift with respect to those of the BTO and STO bulk constituents was found in our experiment. The total thickness of our superlattices was $\sim$ 250 nm, i.e., far

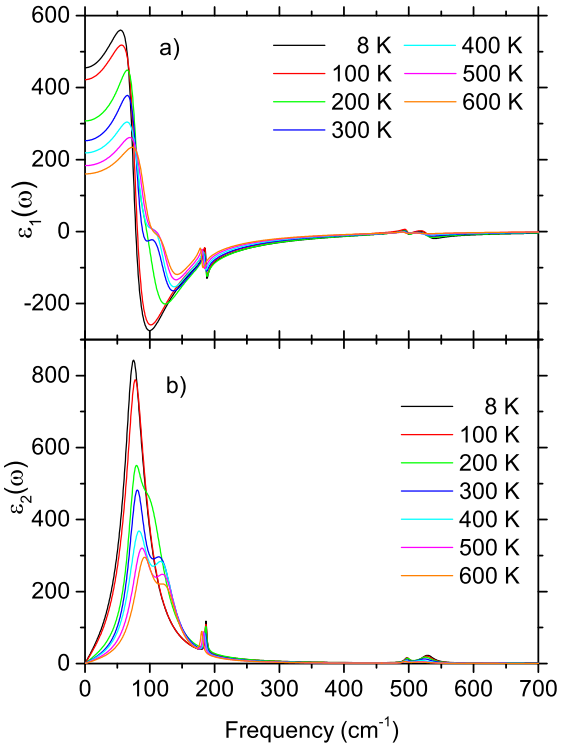


FIG. 6: (color online)Temperature dependence of the real (panel a) and imaginary (panel b) parts of the dielectric function of the $(BTO)_8/(STO)_4$ superlattice.

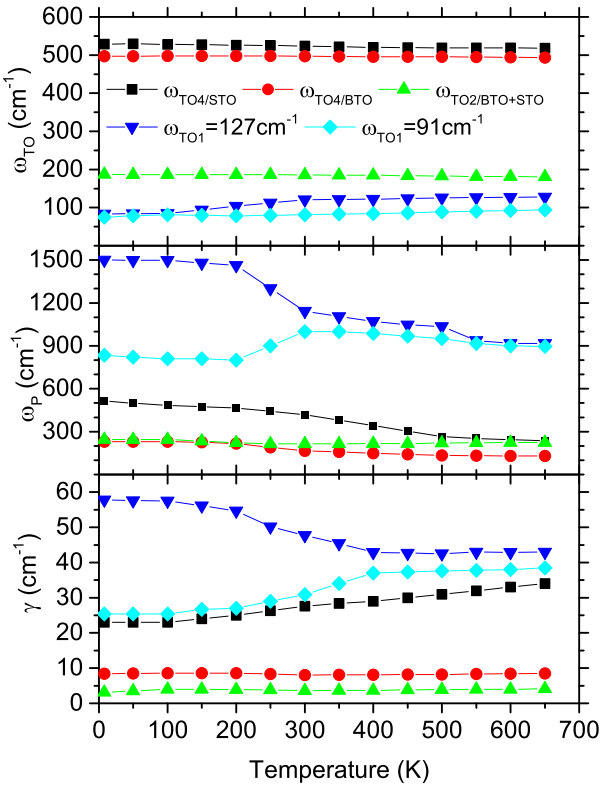


FIG. 7: (color online)Temperature dependence of the phonon parameters $\omega_{TOj}$, $\omega_{Pj}$, and $\gamma_j$ used to the fit of infrared reflectance of the $(BTO)_8/(STO)_4$ superlattice on a (110) DSO substrate.

greater than very thin films (∼10-20 nm) of other studies in which frequency shifts were observed[40,43]. The behavior of our $(BTO)_8/(STO)_4$ superlattice is, therefore, quite different from thin films.

The BST-$x$ solid solution has a complicated phase diagram, which for $x \geq 0.2$ is similar to that of pure BTO, but with its phase transitions shifted to lower temperatures[44,45]. X-ray diffraction and other studies in the literature[46–48] clearly indicate that BST-$x$ with the same overall composition (x=0.67) as our $(BTO)_8/(STO)_4$ superlattice has three phase transitions at about 150, 210 and 290 K.

As mentioned above, for the superlattices studied, the BTO layers are subject to compressive in-plane strain and the STO layers are subject to tensile in-plane strain. In such a situation first-principles calculations[18,49] predict a spontaneous polarization with components along [001] and [110] in the orthorhombic STO layers, whereas in the tetragonal BTO the polarization should be completely along [001]. Adapting these layers to a superlattice leads to further symmetry lowering to the monoclinic $Cm$ space group. The temperature evolution of the Raman spectra[23,30] shows one phase transition from the cubic to the tetragonal phase, whose temperature depends on the substrate-induced strain and the ratio of the BTO and STO constituent layers. For the superlattice with our parameters, $T_C$ was found from Raman to be about 580 K. This is in reasonable agreement with our x-ray and infrared measurements that indicate the same phase transition at about 550 K[23]. Preliminary Raman measurements on a $(BTO)_8/(STO)_4$ superlattice on (110) DSO indicated another phase transition at about 180 K[50]. Its in-plane component of spontaneous polarization is, however, of rather small magnitude. In our spectra this second phase transition manifests itself by the anomalous behavior of the soft mode parameters between 200 and 300 K.

Our fitting procedure reveals that a minimum of five polar phonons are sufficient to describe the reflectance spectrum. The temperature evolution of the parameters obtained from our fitting procedure is shown in Fig. 7. The dielectric function of the superlattice was obtained considering it as an effective medium using Eq. 6. This approximation is directly applicable for acoustic phonons, which for $k \approx 0$ have linear dispersion and propagate homogeneously through the entire sample, but with different velocities in the BTO and STO layers. This results in their simple folding. The optic phonons in the superlattice also fold, but they have rather different features: they form narrow bands which are nearly flat and

are not overlapping. The phonons can propagate only in one of the constituent layers. Their properties cannot be taken as the average of both constituents and are referred to as confined modes.

Depending on the degree of confinement, the optic phonons in superlattices can, in an analogous way to their behavior in solid solutions, exhibit either so-called one-mode or two-mode behavior. Our BTO/STO superlattices serves as a good example. Knowing Servion's data for bulk BTO[51] and STO[52] we can make mode assignments. The highest frequency, TO4, modes are found at 485 $cm^{-1}$ for BTO and 545 $cm^{-1}$ for STO in pure bulk compounds. In the superlattice they are shifted to 496 $cm^{-1}$ and 524 $cm^{-1}$, respectively. They have very flat dispersion and their frequencies are sufficiently far from each other to avoid overlap. They show two-mode-like behavior with clearly distinguished peaks for BTO-like and STO-like confined phonons in the corresponding layers. Quite opposite behavior is observed for TO2 phonons with pure component frequencies 181 $cm^{-1}$ and 175 $cm^{-1}$ for BTO and STO, respectively. They nearly overlap and they form just one peak in the observed spectrum of our superlattice at the frequency 180 $cm^{-1}$. The frequencies of both the TO2 and TO4 phonons are practically independent of temperature.

The behavior of the TO1 phonons, which are so-called soft phonons, is more complicated. This is because the $E$-polarized soft mode in bulk BTO has a very strong oscillator strength and is overdamped[51]. Its parameters, therefore, can be hardly determined even for a bulk sample. At high temperature in our $(BTO)_8/(STO)_4$ superlattice it is possible to easily distinguish between the two TO1 soft modes at 93 $cm^{-1}$ and 127 $cm^{-1}$ whose frequencies slowly decrease on cooling as it is shown in Fig. 7. Our X-ray diffraction data show a change of slope in the temperature dependence of the out-of-plane lattice parameter at about 550 K indicating a phase transition. At the same temperature an increase in reflectance in the frequency region of the soft mode $\sim$100 $cm^{-1}$ and its oscillator strength is also observed. There is, however, no typical phonon softening known for bulk materials. Nevertheless, this behavior can be explained. Our superlattice in the whole measured temperature interval is in the tetragonal phase as it is shown in Fig. 2. At 550 K it only elongates along the c-axis. The in-plane atomic positions being fixed and only an out-of-plane extension of the lattice parameters occurs. The transformation proceeds only in the direction perpendicular to the superlattice layers. The atomic displacement connected with this transformation can be, therefore, hardly reflected by the $E$-polarized phonons and their complete softening expected. The frequencies of the two soft modes approach each other below room temperature and also the oscillator strength of the higher-frequency mode starts to transfer to the lower-frequency mode. Finally, at low temperature, below 200 K, the low-frequency mode stops softening, both modes practically coalesce and finally only one mode is observed with larger oscillator strength and broadening, as can be seen in Fig. 6. The frequency softening of this combined mode is not complete, but it stops at 78 $cm^{-1}$. This behavior is connected with the existence of another phase transition, which was reported, but never published[50]. Both phase transitions show in infrared spectra only by the changes of the soft phonon oscillator strengthes. A similar behavior in Raman spectra has been observed for TO2 and TO4 phonons[23]. Our finding is also consistent with the hardening of soft modes well-established in thin films[43,53], where the softening stops at 63 $cm^{-1}$ and it is explained by the influence of oxygen vacancies or strain on the soft mode behavior.

The static dielectric function, Eq. 3, consists of the contribution of $\varepsilon_\infty$ arising from the electronic response and the contribution obtained by summing the contributions, $\Delta\varepsilon_j$, of all infrared-active phonons, which scale as $\omega_{Pj}^2/\omega_{TOj}^2$. It is also equal to $\Omega_0^2\tilde{Z}_j^{*2}/\omega_{TOj}^2$, where $\Omega_0^2 = 4\pi e^2/V_{cell}M$, $\omega_{Pj}$ is the unscreened plasma phonon frequency, $\tilde{Z}_j^*$ is the mode effective charge, $\omega_{TOj}$ is the resonance frequency of the $j$-th mode, and $M$ is the atomic mass unit[54,55]. The Lyddane-Sachs-Teller relation implies that the existence of at least one low-frequency mode with large $\tilde{Z}_j^*$ is needed to yield a large dielectric constant. In our case as temperature is varied, the total phonon contribution to the static permittivity $\varepsilon_0 = \varepsilon_\infty + \Sigma\Delta\varepsilon_j$ varies from about 200 at 650 K to about 450 at 8 K. This value is still about one half of the value measured in the microwave frequency region[56]. This shows that there are other low-frequency contributions to permittivity.

One of the mechanisms that can increase the static permittivity of ferroelectric superlattices depends on the activation of folded acoustic phonons. A similar effect has been observed in the infrared reflectance of CdS/CdSe[57] and GaN/AlN[58] superlattices. In our spectra it manifests itself in the low-frequency region, where a W-shaped spectral feature with minima at 33 and 54 $cm^{-1}$ is clearly seen. These positions are quite close to the frequencies where folded acoustic phonons have been found by Raman scattering[59,60] in BTO/STO superlattices.

The piezoelectric constants of ferroelectrics are about by one order stronger than those of semiconductors[61]. The stress and strain generated by acoustic waves produce electric polarization through the direct piezoelectric effect. It enables the coupling of the polarization to electromagnetic radiation. The additional periodicity imposed by the superlattice structure causes folding of the Brillouin zone and some of the points of the phonon branches ending up at k=0 become optically active[62]. As the modulation in our superlattice is of nanoscopic scale the frequency of piezoelectric resonance shifts to the terahertz region and can be observed in infrared spectra.

Our low-frequency reflectance spectra are shown in Fig. 8. The oscillations in the spectra are the Fabry-Perot interferences caused by multiple reflection in the DSO substrate. In our spectra only one doublet of acoustic phonons is seen in contrast with semiconductor superlattices. The higher-order modes can not be observed

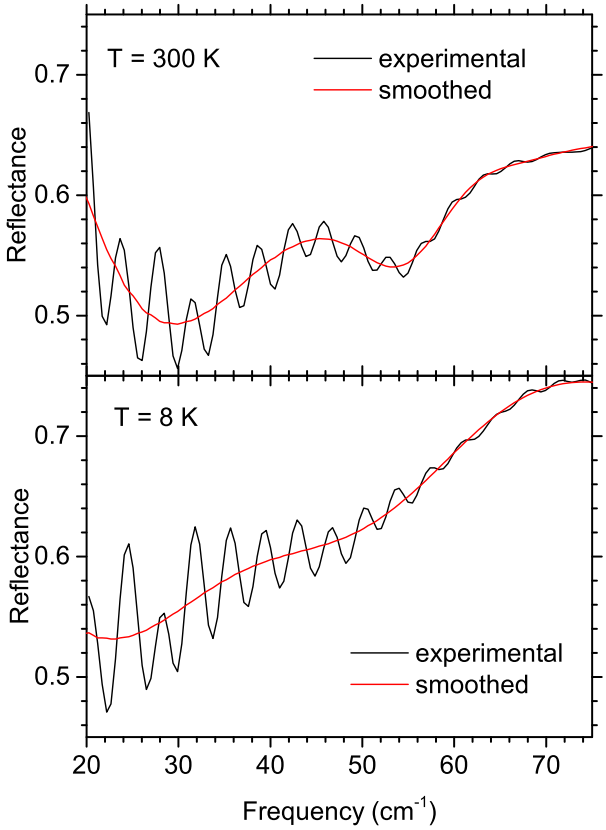


FIG. 8: (color online)Low-frequency reflectance at 8 and 300 K showing the first order acoustic phonons. The spectra were also smoothed to stress the role of the acoustic phonons features.

because they are overlaid by the soft mode, which represents itself in Fig. 8 as an continuum increasing with frequency. When the temperature decreases below 150 K, the frequency of the soft phonon decreases and its oscillator strength increases, and the soft mode practically screens also the first order acoustic phonons as it is seen in the lower panel at 8 K. This is the reason why it is not possible to study their temperature dependence. On the other hand at room temperature it is possible to estimate their contribution to the static permittivity. Its value increases and almost approaches the value measured in the microwave frequency region[56].

## IV. CONCLUSIONS

The polarized infrared reflectance of a $(BTO)_8/(STO)_4$ superlattice grown on a (110) DSO substrate was studied over the broad temperature range 8 - 650 K. Using the effective medium approximation for multilayers systems and the Drude-Lorentz formula for their dispersion, we simulated the far-infrared reflectance of the structures and thus extracted the phonon parameters and determined the dielectric function of the $(BTO)_8/(STO)_4$ superlattice. This dielectric function shows typical perovskite features with three infrared active phonons coming from each component layer. As the $(BTO)_8/(STO)_4$ superlattice consists of two components, two phonons show two-mode behavior and one phonon shows one-mode behavior. The most significant feature in the spectrum is a peak at around 100 $cm^{-1}$, which begins to increase below 550 K. It corresponds to the polar phonon with the lowest frequency in perovskite structures and in bulk materials it is considered to be a soft mode. In our case, practically no softening is observed and the phonon frequency keeps approximately the same value and only its intensity increases on cooling. The appearance of this peak at 100 $cm^{-1}$coincides with an increase in the out-of-plane lattice parameter measured by x-ray diffraction at around 550 K. Using infrared spectroscopy we can identify this as an ferroelectric phase transition into a tetragonal phase. This phase transition occurs nearly 150 K higher in temperature than it does in (unstrained) bulk BTO , but comparable to where it occurs (∼540°C) in BTO commensurately strained to (110) DSO[17]. Another anomalous behavior is found between 200 and 300 K, where the two low-frequency phonons merge and infrared reflectance increases. At this low temperature a phase transition was also identified by Raman scattering[50].

## V. ACKNOWLEDGMENTS

This work was partially supported by Grant Agency of the Czech Republic under Contract No. 202/07/0591 and by the Ministry of Education of the Czech Republic under Contracts ME08109 and LM2011020. A.S. and D.G.S. gratefully acknowledge the financial support from the National Science Foundation through the MRSEC program (DMR-1420620). This work was performed in part at the Cornell NanoScale Facility, a member of the National Nanotechnology Coordinated Infrastructure (NNCI), which is supported by the National Science Foundation (Grant ECCS-1542081).

* Electronic address: zelezny@fzu.cz

[1] A. Moulson and J. Herbert, *Electroceramics* (John Wiley & Sons Ltd, Chichester, 2006).
[2] Y. Xu, *Ferroelectric Materials and Their Applications* (North-Holland, New York, 1991).

[3] K. Rabe, C. Ahn, and J. Triscone, *Physics of Ferroelectrics: A Modern Perspective*, Topics in Applied Physics (Springer Berlin Heidelberg, 2007), ISBN 9783540345916, URL https://books.google.cz/books?id=CWTzxRCDJdMC.

[4] J. F. Scott, ISRN Materials Science **2013**, 187313 (2013).

[5] T. Shimuta, O. Nakagawara, T. Makino, S. Arai, H. Tabata, and T. Kawai, J. Appl. Phys. **91**, 2290 (2002).

[6] L. Kim, D. Jung, J. Kim, Y. S. Kim, and J. Lee, Appl. Phys. Lett. **82**, 2118 (2003).

[7] W. Tian, J. Jiang, X. Pan, J. Haeni, Y. Li, L. Chen, D. Schlom, J. Neaton, K. Rabe, and Q. Jia, Appl. Phys. Lett. **89**, 092905 (2006).

[8] H. N. Lee, H. M. Christen, M. F. Chisholm, C. M. Rouleau, and D. H. Lowndes, Nature **433**, 395 (2005).

[9] M. P. Warusawithana, E. V. Colla, J. N. Eckstein, and M. B. Weissman, Phys. Rev. Lett. **90**, 036802 (2003), URL http://link.aps.org/doi/10.1103/PhysRevLett.90.036802.

[10] M. Liu, C. Ma, G. Collins, J. Liu, C. Chen, A. D. Alemayehu, G. Subramanyam, Y. Ding, J. Chen, C. Dai, et al., Nanoscale Research Letters **8**, 1 (2013), ISSN 1556-276X, URL http://dx.doi.org/10.1186/1556-276X-8-338.

[11] L. B. Freund and S. Suresh, *Thin film materials: stress, defect formation and surface evolution* (Cambridge University Press, 2003).

[12] J. S. Speck, A. C. Daykin, A. Seifert, A. E. Romanov, and W. Pompe, J. Appl. Phys. **78** (1995).

[13] W. Nix and B. Clemens, J. Mater. Res. **14**, 3467 (1999).

[14] T. R. Taylor, P. J. Hansen, B. Acikel, N. Pervez, R. A. York, S. K. Streiffer, and J. S. Speck, Appl. Phys. Lett. **80** (2002).

[15] D. G. Schlom, L.-Q. Chen, C.-B. Eom, K. M. Rabe, S. K. Streiffer, and J.-M. Triscone, Annual Review of Materials Research **37**, 589 (2007).

[16] J. Haeni, P. Irvin, W. Chang, R. Uecker, P. Reiche, Y. Li, S. Choudhury, W. Tian, H. Hawley, B. Craigo, et al., Nature **430**, 758 (2004).

[17] K. J. Choi, M. Biegalski, Y. Li, A. Sharan, J. Schubert, R. Uecker, P. Reiche, Y. Chen, X. Pan, V. Gopalan, et al., Science **306**, 1005 (2004).

[18] J. B. Neaton and K. M. Rabe, Appl. Phys. Lett. **82** (2003).

[19] C. H. Ahn, K. M. Rabe, and J.-M. Triscone, Science **303**, 488 (2004), ISSN 0036-8075, http://science.sciencemag.org/content/303/5657/488.full.pdf, URL http://science.sciencemag.org/content/303/5657/488.

[20] E. Bousquet, M. Dawber, N. Stucki, C. Lichtensteiger, P. Hermet, S. Gariglio, J.-M. Triscone, and P. Ghosez, Nature **452**, 732 (2008), cited By 328, URL https://www.scopus.com/inward/record.uri?eid=2-s2.0-42149091079&partnerID=40&md5=43068e2dbe4492d5ab69d2cb6f54481d.

[21] D. A. Tenne and X. Xi, J. Am. Ceram. Soc.J. Am. Ceram. Soc. **91**, 1820 (2008).

[22] Y. Yuzyuk, Physics of the Solid State **54**, 1026 (2012), ISSN 1063-7834, URL http://dx.doi.org/10.1134/S1063783412050502.

[23] D. A. Tenne, A. Bruchhausen, N. D. Lanzillotti-Kimura, A. Fainstein, R. S. Katiyar, A. Cantarero, A. Soukiassian, V. Vaithyanathan, J. H. Haeni, W. Tian, et al., Science **313**, 1614 (2006).

[24] J. Schubert, O. Trithaveesak, A. Petraru, C. Jia, R. Uecker, P. Reiche, and D. Schlom, Appl. Phys. Lett. **82**, 3460 (2003).

[25] R. Uecker, H. Wilke, D. Schlom, B. Velickov, P. Reiche, A. Polity, M. Bernhagen, and M. Rossberg, J. Cryst. Growth **295**, 84 (2006).

[26] D. G. Schlom, L.-Q. Chen, C. J. Fennie, V. Gopalan, D. A. Muller, X. Pan, R. Ramesh, and R. Uecker, MRS Bull. **39**, 118 (2014), URL https://www.cambridge.org/core/article/div-class-title-elastic-strain-engineering-of-ferroic-oxides-div/E1607637781B539C31D5149282AC81A8.

[27] D. O'Neill, R. M. Bowman, and J. M. Gregg, Appl. Phys. Lett. **77**, 1520 (2000), http://aip.scitation.org/doi/pdf/10.1063/1.1290691, URL http://aip.scitation.org/doi/abs/10.1063/1.1290691.

[28] G. Catalan, D. O'Neill, R. M. Bowman, and J. M. Gregg, Appl. Phys. Lett. **77**, 3078 (2000), http://aip.scitation.org/doi/pdf/10.1063/1.1324729, URL http://aip.scitation.org/doi/abs/10.1063/1.1324729.

[29] D. Schlom, J. Haeni, J. Lettieri, C. Theis, W. Tian, J. Jiang, and X. Pan, Materials Science and Engineering: B **87**, 282 (2001), ISSN 0921-5107, URL http://www.sciencedirect.com/science/article/pii/S0921510701007267.

[30] A. Soukiassian, W. Tian, V. Vaithyanathan, J. H. L. Chen, X. Xi, D. Schlom, D. Tenne, H. Sun, X. Pan, K. Choi, et al., J. Mater. Res. **23**, 1417 (2008).

[31] Y. L. Li, S. Y. Hu, D. Tenne, A. Soukiassian, D. G. Schlom, L. Q. Chen, X. X. Xi, K. J. Choi, C. B. Eom, A. Saxena, et al., Appl. Phys. Lett. **91**, 252904 (2007), URL http://scitation.aip.org/content/aip/journal/apl/91/25/10.1063/1.2823608.

[32] Y. L. Li, S. Y. Hu, D. Tenne, A. Soukiassian, D. G. Schlom, X. X. Xi, K. J. Choi, C. B. Eom, A. Saxena, T. Lookman, et al., Appl. Phys. Lett. **91**, 112914 (2007), URL http://scitation.aip.org/content/aip/journal/apl/91/11/10.1063/1.2785121.

[33] O. S. Heavens, *Optical Properties on thin Solid films* (DoverPublications. com, 1955).

[34] W. Vriens and W. Rippens, Appl.Opt. **22**, 4105 (1983).

[35] V. Železný, I. Fedorov, and J. Petzelt, Czechoslovak Journal of Physics **48**, 537 (1998), ISSN 1572-9486, URL http://dx.doi.org/10.1023/A:1021213002432.

[36] J. Hlinka, V. Železný, S. M. Nakhmanson, A. Soukiassian, X. X. Xi, and D. G. Schlom, Phys. Rev. B **82**, 224102 (2010).

[37] B. Veličkov, V. Kahlenberg, R. Bertram, and M. Bernhagen, Zeitschrift für Kristallographie **222**, 466 (2007).

[38] M. Biegalski, J. Haeni, S. Trolier-McKinstry, D. Schlom, C. Brandle, and A. V. Graitis, Journal of Materials Research **20**, 952 (2005), URL https://www.cambridge.org/core/article/div-class-title-rmal-expansion-of-the-new-perovskite-substrates-dysco-span-class-sub-3-span-and-gdsco-span-class-s

B101BB948EDAC35FDAC8106A96170089.
[39] S. Kamba, V. Goian, D. Nuzhnyy, V. Bovtun, M. Kempa, J. Prokleška, M. Bernhagen, R. Uecker, and D. G. Schlom, Phase Transitions **86**, 206 (2013).
[40] D. Nuzhnyy, J. Petzelt, S. Kamba, P. Kužel, C. Kadlec, V. Bovtun, M. Kempa, J. Schubert, C. Brooks, and D. Schlom, Appl. Phys. Lett **95**, 232902 (2009).
[41] G. A. Komandin, E. S. Zhukova, V. I. Torgashev, A. V. Boris, A. A. Boris, E. A. Motovilova, A. S. Prokhorov, L. S. Kadyrov, B. P. Gorshunov, and M. Dressel, J. Appl. Phys. **114**, 024102 (2013).
[42] S. Coh, T. Heeg, J. H. Haeni, M. D. Biegalski, J. Lettieri, L. F. Edge, K. E. O'Brien, M. Bernhagen, P. Reiche, R. Uecker, et al., Phys. Rev. B **82**, 064101 (2010), supplementary information about the calculated phonon parameters is available at http://link.aps.org/doi/10.1103/PhysRevB.82.064101/supp.pdf.
[43] T. Ostapchuk, J. Petzelt, V. Železný, A. Pashkin, J. Pokorný, I. Drbohlav, R. Kužel, D. Rafaja, B. Gorshunov, M. Dressel, et al., Phys. Rev. B **66**, 235406 (2002).
[44] V. V. Lemanov, E. P. Smirnova, P. P. Syrnikov, and E. A. Tarakanov, Phys. Rev. B **54**, 3151 (1996).
[45] V. B. Shirokov, V. I. Torgashev, A. A. Bakirov, and V. V. Lemanov, Phys. Rev. B **73**, 104116 (2006).
[46] D. A. Tenne, A. M. Clark, A. R. James, A. Soukiassian, K. Chen, and X. X. Xi, MRS Proceedings **688** (2001).
[47] Y. I. Yuzyuk, J. Sauvajol, P. Simon, V. Lorman, V. Alyoshin, I. Zakharchenko, and E. Sviridov, J. Appl. Phys. **93**, 9930 (2003).
[48] D. A. Tenne, A. Soukiassian, M. H. Zhu, A. M. Clark, X. X. Xi, H. Choosuwan, Q. He, R. Guo, and A. S. Bhalla, Phys. Rev. B **67**, 012302 (2003), URL http://link.aps.org/doi/10.1103/PhysRevB.67.012302.
[49] K. Johnston, X. Huang, J. B. Neaton, and K. M. Rabe, Phys. Rev. B **71**, 100103 (2005).
[50] D. A. Tenne, J. D. Schmidt, P. Turner, A. Soukiassian, D. G. Schlom, S. Nakhmanson, X. X. Xi, Y. L. Li, L. Q. Chen, R. S. Katiyar, et al., poster Presentation at Workshop on the Fundamental Physics of Ferroelectrics, Williamsburg, Virginia, 8–11 February 2009 (unpublished); D. A. Tenne, J. D. Schmidt, P. Turner, A. Soukiassian, D. G. Schlom, S. Nakhmanson, X. X. Xi, Y. L. Li, L. Q. Chen, and R. S. Katiyar, et al., APS March Meeting, 16–20 March 2009 (unpublished).
[51] J. L. Servoin, F. Gervais, A. M. Quittet, and Y. Luspin, Phys. Rev. B **21**, 2038 (1980), URL http://link.aps.org/doi/10.1103/PhysRevB.21.2038.
[52] J. L. Servoin, Y. Luspin, and F. Gervais, Phys. Rev. B **22**, 5501 (1980), URL http://link.aps.org/doi/10.1103/PhysRevB.22.5501.
[53] A. Sirenko, C. Bernhard, A. Golnik, A. M. Clark, J. Hao, W. Si, and X. Xi, Nature **404**, 373 (2000).
[54] W. Zhong, R. D. King-Smith, and D. Vanderbilt, Phys. Rev. Lett. **72**, 3618 (1994).
[55] X. Gonze and C. Lee, Phys. Rev. B **55**, 10355 (1997).
[56] M. Liu, C. Ma, G. Collins, J. Liu, C. Chen, C. Dai, Y. Lin, L. Shui, F. Xiang, H. Wang, et al., ACS Applied Materials & Interfaces **4**, 5761 (2012), http://dx.doi.org/10.1021/am301066u, URL http://dx.doi.org/10.1021/am301066u.
[57] M. Göppert, M. Hetterich, A. Dinger, C. Klingshirn, and K. P. O'Donnell, Phys. Rev. B **57**, 13068 (1998), URL http://link.aps.org/doi/10.1103/PhysRevB.57.13068.
[58] C. Aku-Leh, K. Reimann, M. Woerner, E. Monroy, and D. Hofstetter, Phys. Rev. B **85**, 155323 (2012), URL http://link.aps.org/doi/10.1103/PhysRevB.85.155323.
[59] A. Bruchhausen, A. Fainstein, A. Soukiassian, D. G. Schlom, X. X. Xi, M. Bernhagen, P. Reiche, and R. Uecker, Phys. Rev. Lett. **101**, 197402 (2008).
[60] R. R. Das, Y. I. Yuzyuk, P. Bhattacharya, V. Gupta, and R. S. Katiyar, Phys. Rev. B **69**, 132302 (2004), URL http://link.aps.org/doi/10.1103/PhysRevB.69.132302.
[61] R. E. Newnham, *Structure-property relations* (Springer Science & Business Media, 2012).
[62] A. Bruchhausen, N. D. Lanzillotti-Kimura, A. Fainstein, A. Soukiassian, D. A. Tenne, D. Schlom, X. X. Xi, and A. Cantarero, Journal of Physics: Conference Series **92**, 012160 (2007), URL http://stacks.iop.org/1742-6596/92/i=1/a=012160.